A molecular dynamics simulation of pressure-driven gas permeation in a micropore potential field on silica membranes

Tomohisa Yoshioka*, Masashi Asaeda, Toshinori Tsuru
Department of Chemical Engineering, Hiroshima University, Higashi-Hiroshima, 739-8527, Japan

*Corresponding author;
Tel.: +81-824-424-7719, Fax.: +81-424-5494,
E-mail: tom@hiroshima-u.ac.jp (Tomohisa Yoshioka)

Abstract
The mechanisms involved in pressure driven gas permeation through a micropore on vitreous SiO_2 membranes were examined molecular dynamics (MD) simulation. Virtual amorphous SiO_2 membranes were prepared by the melt-quench method utilizing modified Born-Mayer-Huggins (BMH) pair potential and Stillinger-Weber (SW) three-body interactions. A dual control plane non-equilibrium MD (DCP-NEMD) technique was employed to simulate gas permeation phenomena under a constant upstream pressure, in which the permeating molecules were modeled as Lennard-Jones particles. The dependencies of the permeance of helium and CO_2 molecules on temperature and pore size were examined. For cylindrical pores about 8 and 6 Å in diameter, the calculated temperature dependencies for the permeance of helium molecules were similar to the tendencies predicted by the normal Knudsen permeation mechanism, while in the case of CO_2 permeation, a temperature dependency larger than helium and a significant deviation from the Knudsen mechanism were observed. The deviation was more obvious for the smaller 6 Å pore model. A simple gas permeation model that takes the effect of the pore wall potential field into consideration satisfactorily explained the permeation properties of CO_2 in the high temperature region. The permeation mechanism was also examined from the viewpoint of the lateral potential and density distribution in a micropore. The values for the potential within micropores, predicted from the observed temperature dependencies of the gas permeation rate and using the simple gas permeation model, were in good agreement with the depth of the potential field resulting from the given potential parameters. The findings also indicate that the density (pressure) difference in a micropore between the pore entrance and exit, which could be enhanced by an attractive pore wall potential, might be the true driving force for permeation, particularly in the high temperature region.

Keywords: silica membrane, molecular dynamics, gas permeation, micropore

1. Introduction

Separation processes that utilize membrane units have attracted considerable attention because they would not only be effective for the highly selective separation of molecular mixtures, but are also low energy processes. In recent decades, the development of a variety of porous inorganic membranes such as sol-gel derived ceramic membranes, CVD modified membranes, and zeolite membranes etc., which have pores of the same order as the molecular size, has been reported [1]. Since such porous inorganic membranes have relatively good chemical and thermal resistance, it would be predicted that they could be used under severe conditions.

In order to design a porous inorganic membrane unit and to determine the optimum operating conditions for such separation processes, a knowledge of the transport mechanisms of molecules within micropores is necessary. Gas transport mechanisms through polymeric membranes are recognized as solution and diffusion processes. On the other hand, for inorganic porous membranes which have rigid and stable porous structures, gases permeate through narrow but permanent open spaces. A qualitative and quantitative understanding of the transport mechanisms of molecules through such a limited space is important from both the viewpoint of scientific interest and engineering demands for the development of inorganic molecular separation membranes. The mechanism of gas permeation for microporous inorganic membranes has been studied using zeolite or modified glass membranes by many groups [1-5]. However, in terms of the theoretical treatment of observed experimental results, difficulties as the result of uncertainties associated with the characteristics of porous structures, such as the effects of pore size distribution and the presence of unexpected large pinholes have always existed.

On the other hand, using molecular simulation as an ideal experimental system, the microstructure of a system could be examined on a molecular scale. This type of simulation method has been used to predict physical properties, material design and the verification of theories in several fields. In order to quantitatively predict and verify events that occur on a nano- or subnano-scale, it is highly desirable to avoid the uncertainties associated with a real experimental system. From this point of view, a study of molecular permeation through microporous membranes by means of molecular simulation would be very helpful.

After molecular dynamics (MD) and Monte Carlo (MC) simulations concerning phase equilibrium were conducted by many research groups, simulation techniques, which enable the non-equilibrium state to be simulated, were developed using the molecular dynamics method (NEMD). In the last decade, such NEMD simulation methods have been adopted to investigate the pressure- or density-driven transport of molecules through the pores of porous materials. Heffelfinger et al. simulated molecular transport driven by a chemical potential gradient using the newly developed dual control volume grand canonical molecular dynamics (DCV-GCMD) [6-8]. Furukawa et al. also developed a new NEMD simulation technique named μVT-NEMD for simulating gas permeation through a carbon slit pore, based on selective adsorption and surface diffusion mechanisms, by combining the grand canonical ensemble Monte Carlo technique and a boundary-driven NEMD method [9]. At almost the same time, gradient-driven gas diffusion simulations in pores were examined by other groups [10,11]. Several such NEMD simulation methods which use an MD cell combined with a grand canonical Monte Carlo simulation cell have been applied to the simulation of molecular permeation through porous membranes or narrow pores [12-17]. Concerning realistic membrane separation simulation using the DCV-NEMD technique, Wang et al. reported that an iteration process according to permeation performance was necessary [18]. These types of simulations provide valuable information on the transport phenomena of molecules through micropores.

We previously presented papers in which the GC-like MD technique [12,13] was applied to gas permeation simulations through microporous silica membranes [19,20,21]. In this study, we also prepared virtual amorphous silica membranes which had pores that were subnano-scale in diameter, and examined pressure gradient driven gas permeation phenomena through the micropores. One of the objectives of this paper was to describe the details of this simulation method, referred to as "DCP-NEMD", by investigating changes in the number of permeated gas molecules and velocity distributions of gas molecules near an imaginary boundary plane with the bulk gas phase. The other was to study the relation between gas permeation properties and the external potential in a micropore by investigating the density profile of permeating molecules along the flow direction and the pore size dependency of the potential depth in micropores. We previously proposed a simple gas permeation model developed by considering the effect of pore wall potential on gas permeation properties through a micropore, which was examined for real sol-gel derived silica membranes [2]. Using the MD simulation as an ideal experimental system, microporous membranes of any well defined desired pore size can be prepared via a computer and detailed information on gas permeation behavior can be obtained from a microscopic point of view. The model was examined and verified by analyzing the simulated temperature and pore size dependency for the gas permeation rate for helium and CO_2-like LJ particles as permeants.

2. Simulation scheme

The ideal experimental system used here consisted of a microporous membrane unit and permeating gas molecules. The membrane material was amorphous silica, consisting of silicon and oxygen atoms, and the permeating gas molecules were helium-like and CO_2-like LJ particles. The following three types of functions were used as potential functions. In order to simulate an amorphous silica structure, we employed two types of functions. One was the modified BMH (Born-Mayer-Huggins) pair potential given by Eq. (1) [22],

$$\phi_2(r_{ij}) = A_{ij} \exp\left[\frac{-r_{ij}}{\rho}\right] + \frac{z_i z_j e^2}{4\pi\varepsilon_0 r_{ij}} \operatorname{erfc}\left(\frac{r_{ij}}{\beta_{ij}}\right), \tag{1}$$

where r_{ij} is the inter-particle separation distance, Z_i the formal ionic charge, A_{ij} and ρ the parameters of the short-range repulsive term, and β_{ij} describes the range of Coulombic interactions. This is a two-body potential for Si-Si, Si-O and O-O atom pairs as a function of inter-particle distance and formal ionic charges. Another was the SW (Stillinger-Weber) potential described by Eq. (2) [18],

$$\phi_3(r_{ij}, r_{ik}, \theta_{ijk}) = \begin{cases} \lambda_i \exp\left(\dfrac{\gamma_i}{r_{ij} - r_i^c} + \dfrac{\gamma_i}{r_{ik} - r_i^c}\right)\left(\cos\theta_{jik} - \cos\theta_{jik}^c\right)^2, & r_{ij} < r_i^c \text{ and } r_{ik} < r_i^c \\ 0, & r_{ij} \geq r_i^c \text{ or } r_{ik} \geq r_i^c \end{cases}, \tag{2}$$

This is a three-body potential for O-Si-O and Si-O-Si atom bonds as a function of two inter-particle distances r_{ij}, r_{ik} and bond angle θ_{jik}. For interactions among permeating gas molecules, and between gas molecules and oxygen atoms on a membrane, the widely known Lennard-Jones potential, given by Eq. (3), was used.

$$E(r_{ij}) = 4\varepsilon_{ij}\left[\left(\frac{\sigma_{ij}}{r_{ij}}\right)^{12} - \left(\frac{\sigma_{ij}}{r_{ij}}\right)^{6}\right], \tag{3}$$

Our simulation consisted of two steps, that is, a membrane preparation stage and a gas permeation stage. Figure 1 shows the procedure used to prepare a virtual amorphous silica

membrane. Details of the procedures for obtaining bulk amorphous silica structures were the same as those reported by Feuston and Garofalini [18]. An MD cell starting from a cristobalite crystalline structure consisting of 512 silicon and 1024 oxygen atoms, was melted at 6000 K by periodic velocity scaling during the first 200 ps. The system was then cooled stepwise to 300 K to give a bulk amorphous silica structure, achieving an internal equilibrium at intermediate temperatures of 4000, 2000, and 1000 K. The averaged cooling rate at that period was about 10^{13} K/s. The simulation was performed with periodic boundary conditions in three (*x*, *y*, and *z*) directions. The volume of the MD cell was determined so as to correspond to the actual glass density, 2.2 g/cm^3 [23]. A time step of 1 fs was used with the fifth order Gear's algorithm for integrating the equations of motion [24].

Amorphous silica surfaces were produced by removing the periodic boundary condition in the *z*-direction on the bulk body. After forming the membrane surfaces, the system was relaxed at 300 K for 20 ps. The unit was then dug to create a cylindrical pore in the *z*-direction. Through this digging operation, 171 atoms for an 8 Å pore and 92 atoms for a 6 Å pore were removed from the interior of the body. After the pore digging, the system was again relaxed at 300 K for 50 ps. Just after removing the periodic boundary condition or cutting out the pore structure, the newly generated artificial surface of the membrane is unstable. Relaxation at a high temperature in this situation could cause an unreasonable escape of Si and O atoms from the surfaces. Therefore, we conducted the relaxation under relatively mild conditions, at 300 K. The amorphous membrane structure obtained using this procedure, however, showed an RDF similar to that of a bulk amorphous body with the periodic boundary condition. Even when this membrane unit was used in gas permeation simulations at a higher temperature, 800K, no change in structure was observed. As a result, two types of amorphous silica membrane units which had 8 Å and 6 Å cylindrical pore diameters, respectively, were obtained. These simulation systems were about 28.5 Å in length in the *x*, *y*, and *z* directions, that is the length of the pore or the thickness of these membranes was 28.5 Å. Periodic boundary conditions still remained in the *x* and *y* direction, while was not employed in the direction of permeation (*z*-direction). Sol-gel derived microporous amorphous silica membranes have mostly two types of pores which are effective for gas separation. One is a small opening among the siloxane polymer chains on the dense phase occupying a major area of the membrane surface, where only small molecules such as He and H_2 can manage to pass through. The other is a larger inter-particle pore originating from a space between silica colloidal particles through which N_2, CO_2, and light hydrocarbons can permeate. Our membrane models, which were prepared by cutting out the pore structure imitate the latter inter-particle pores, but not openings in the dense phase. It is very important to reveal gas permeation properties in a subnano-scale inter-particle pore as elemental phenomena for an understanding of overall gas permeation and separation properties through bi-modal porous structural ceramic membranes.

Some important demands for the gas permeation simulation scheme were that it should provide information concerning permeation properties at the steady state, for example, the temperature dependency of permeance and the density profile within a micropore in the direction of flow. In order to obtain the above information, an NEMD simulation involving changing in the number of molecules in the system must be conducted, to attain the steady state with given upstream and downstream conditions, to maintain the chemical potential gradient in the system. In general, the non-equilibrium GCMD method, which utilizes a "hybrid system" of GCMC and *NVT*-MD, is frequently used for dynamical simulations of gas permeation through porous membranes. In this method, high density and low density regions, which are referred to as dual control volumes, are settled at each end of a simulation cell, and the GCMC simulation is conducted in these two regions under the given conditions

in order to prepare the given constant chemical potential regions; a high density or pressure region in the upstream side and a low density or pressure region in the down stream side. At this time, the thermodynamic equilibrium state between each GCMC unit cell and the neighboring side of the MD unit cell is completed, and molecules generated in the GCMC unit cells are transported from the high density region to the lower one, along with the chemical potential gradient through the MD simulation cell. Using the above DCV-GCMD method, however, it is necessary to adopt a large MC:MD ratio in order to obtain an accurate transport coefficient and this leads to an increase in the overall cost of the calculation [25].

As a special case, when the density of the control volume is relatively low, interactions among molecules can be neglected and the fluid in the CV can be approximated as an ideal gas. In this case, the frequency of molecules per unit area and time, which pass through a plane settled in the gas phase can be given, based on the kinetic theory of ideal gases as a function of temperature, pressure and molecular weight. Ford et al. adopted "the plane method" to produce gas phase molecules for investigating the surface barrier effect in the penetration of dilute gas molecules through the pore mouth [26]. Gas molecules were randomly assigned initial *x* and *y* positions in the plane settled at $z = 3.5\sigma$, the distance from the pore mouth. Their initial velocities were chosen from the subset of the Maxwell-Boltzmann distribution which includes only negative *z* velocities at the specified temperature. Miyahara et al. also settled the boundary plane with an imaginary gas phase at both the edges of an MD simulation cell, and by generating molecules on the boundary planes at a frequency corresponding to the desired gas phase pressure, conducted a GC-like MD simulation of the adsorption processes into slit-like nano-pores [12]. In this study, we also introduced boundary planes with an imaginary gas phase corresponding to the high density and low density side of the simulation cell, on which the permeating gas molecules could be generated or deleted. That is, permeating molecules were introduced from the gas phase to the MD simulation cell at a given frequency, and molecules that reached those boundary planes after permeating through the membrane to the downstream region or rebounding on the membrane surface back upstream were deleted. This simulation technique enables an NEMD simulation of pressure driven gas permeation phenomenon under conditions of a constant chemical potential gradient to be easily carried out. Since the chemical potential gradient is maintained not by an insertion and deletion process in the two control volumes but by yielding and deleting molecules on two imaginary border planes with the gas phase, it can be designated as a dual control plane non-equilibrium molecular dynamics (DCP-NEMD) method. This technique is based on the concept of the GC-like MD method [12], and we first successfully applied it to the study of CO_2 permeation in a micropore [19].

Figure 2 shows a schematic image of the simulation cell used for the DCP-NEMD simulations. Gas molecules permeate through the pore on the membrane part in the *z*-direction from the right-hand side to the left-hand side. Control planes on the imaginary gas phase were set at each end at sufficient distances (30 Å) from the membrane surfaces. It should be noted that the artificial "Potential Buffering Field" used in Miyahara's simulation was not necessary for our simulation because the potential gradient from a membrane surface to the gas phase formed spontaneously. Gas molecules were introduced from the control plane such that the frequency, *f* (molecules/sec.) corresponded to the value under the specified temperature and upstream pressure described by Eq. (4) as a function of gas phase pressure *p*, temperature *T*, molecular weight *m* and the area of control plane *S*.

$$f = \frac{pS}{(2\pi mkT)^{0.5}} \tag{4}$$

The position of a newly created molecule on a control plane was randomly chosen. The initial velocity components of a generated molecule were given based on the kinetic theory of

gas, that is, based on the Maxwell-Boltzmann distribution theorem given by Eq. (5), for both the *x* and *y* components, which is perpendicular to the direction of flow.

$$f(v_i) = \left(\frac{m}{2\pi kT}\right)^{0.5} \exp\left(-\frac{mv_i^2}{2kT}\right), (i = x, y) \quad (5)$$

On the contrary, the *z* component of the velocity distribution of molecules that are entering or leaving the simulation cell must be different from a bare Maxwell-Boltzmann distribution since the distribution is a restricted one that should be appropriate for molecules running in the direction of flow. The velocity distribution $f(v_z)$ of molecules with such a restriction is given by Eq. (6).

$$f(v_z) = \frac{m}{kT} v_z \exp\left(-\frac{mv_z^2}{2kT}\right), \quad (6)$$

We gave v_z with the probability of Eq. (6) to a newly created molecule at the control plane.

The forces acting on the permeating molecules in a pore are the result of permeant-permeant molecular and permeant-"silica framework" interactions. The permeating molecules were helium and carbon dioxide which were modeled as Lennard-Jones particles. The permeant molecules were assumed to interact with oxygen atoms on the silica and forces originating from silicon atoms were neglected. To find the CO_2-O and He-O potential parameters, the Lorentz-Berthelot combining rules were used. All potential parameters used in our simulations are summarized in Table 1 and are also listed in reference 18 (modified BMH potential parameters for Si-Si, Si-O, O-O, and SW ones for O-S-O, Si-O-Si), reference 19 (LJ potential parameters for bO, nbO), and reference 3 (LJ potential parameters for He, CO_2), where bO and nbO indicate bridging oxygen (Si-O-Si) and non-bridging oxygen (Si-OH), respectively. We proceeded with the simulations of the dynamics not only of permeating molecules but of silicon and oxygen atoms on silica membranes, as well.

The temperatures used were 260, 300, 350, 400, 500, 600, and 800 K. The temperature of the simulation system was controlled by the velocity scaling of atoms which constituted the membrane unit to satisfy,

$$\sum \frac{1}{2} m_i v_i^2 = \frac{3}{2} kT_{\text{ref}} \quad (7)$$

where m_i is mass of a silicon or oxygen atom, v_i is the velocity, N is the number of atoms whose velocity should be scaled and T_{ref} is the set-point temperature. We scaled the velocity of some of the silicon and oxygen atoms on membranes using the temperature averaged over 100 steps. The velocities of atoms on the two external membrane surfaces and the pore surface, where they could come into contact with permeating molecules and the kinetic energy of molecules should be exchanged with each other, were not scaled. Only the velocities of about 1000 atoms in the interior of the membrane that were more than 5.5 Å from the membrane surfaces and the pore surface were scaled, where 5.5 Å is the cut-off distance of force for the modified BMH potential between Si-Si, O-O and Si-O atom pairs. On the other hand, concerning the velocities of permeating molecules, they were *never* scaled throughout their lifetimes from generation at a control plane to deletion there after permeation or rebounding on a membrane surface. The temperature control method using velocity scaling is a very simple and effective one but is also an unrealistic artificial operation, the application of which should be avoided, when possible. Therefore, it would be expected that the operations used in this study were not only useful in controlling the temperature of the system suitably but in decreasing the undesirable influences of "scaling" on permeating molecules as well and it would enable more realistic permeation phenomena to be observed

through a micropore.

3. Results and discussion

3.1 Amorphous silica membrane structure

In order to confirm the validity of the amorphous silica membrane structure obtained by the melt-quench method, it was compared with a silica crystal structure. A silica crystal membrane, which had the same size of a cylindrical pore of 8 Å as that of an amorphous membrane, was prepared as follows. At the initial state, silicon and oxygen atoms were arranged so as to achieve a β-cristobalite crystal structure configuration, and the membrane surface was produced by removing the periodic boundary condition in the *z*-direction. After relaxation at 300 K for 50 ps, the unit was then dug to create a cylindrical pore in the *z*-direction and was again relaxed at 300 K for 30 ps to obtain a silica crystal porous membrane.

Figure 3 shows the perspectives for a crystal and a melt-quenched membrane unit with a cylindrical pore looking through a pore from the upstream side. The atoms and atomic bonds are drawn as small dots (Si), circles (O) and sticks, respectively. In a perspective of a "crystal membrane" with a pore, a nearly regular structure can be observed except for a small amount of disorder around the pore surface. On the other hand, in a melt-quenched membrane, the entire structure seems to have an irregularity and it can be seen that not a few non-bridging oxygen atoms project out to the pore space. Therefore, the pore surface of the resulting membrane is not smooth and the profile of the "cylindrical" pore is not a perfect circle but rather distorted.

Figure 4 shows two radial distribution functions for silica structures prepared using different procedures. The intensity curves are drawn against atom pair distances. The broken curve shows the result for a β-cristobalite crystal relaxed at 300 K, while the solid one, for the melt-quench method. This broken curve has larger and narrower peaks in the short distance region compared to the solid one. In addition, the periodic structure can be seen even in the relatively long distance region for the β-cristobalite crystal, while, for the melt-quenched membrane, the long range order structure seems to disappear at distances over 5.5 Å. The structure of the silica crystal prepared by relaxation of β-cristobalite at 300 K is obviously different from the melt-quenched silica structure. Si-O-Si and O-Si-O bond angle distributions were also calculated for both the crystal and melt-quenched structure, and are shown in Fig. 5. In that figure, the difference between the two structures could be clearly observed. The calculated radial distribution function and bond angle distribution for the simulated vitreous silica was compared with that previously reported by Feuston and Garofalini [22], to confirm the adequacy of the amorphous silica structure. It should also be noted that such an amorphous structure was kept steadily in the state with two surfaces and a cylindrical pore, not in the bulk body with periodic boundary conditions. These results prove that the values used for the potential parameters are reasonable and that the melt-quench procedures are suitable for preparing an amorphous silica membrane unit which has a cylindrical pore in the Angstrom order.

Figure 6 shows the pore size distributions for the amorphous and crystal silica structures. These curves were determined by dividing a membrane unit into small bins and determining the largest sphere that could contain each grid point. The number of grid points plotted against the value of the sphere diameter gives the pore size distribution. Those two curves have an almost similar peak at 8 Å, corresponding to a penetrating cylindrical pore. At smaller voids, however, the amorphous silica structure shows a broad distribution curve less than 4 Å, while the crystal structure shows a narrow peak at 2.7 Å and contains no pores larger than 3.3 Å except for the 8 Å pore. The pores or small voids from 3 to 4 Å observed

in the amorphous structure might be called as “fragmental pores” formed by silica polymer chains [21]. For a real sol-gel derived silica membrane, the major area of a membrane surface consists of a fragmental pore phase, and the total volume of the inter-particle pores is very small compared to that for the intra-particle voids. Since a small gas species such as helium (molecular diameter = 2.6 Å) and hydrogen (2.9 Å) could permeate through these voids on real silica membranes, this could explain the excellent permeance and selectivity of He and H_2 over larger molecules which can only permeate through larger inter-particle pores [2]. However, in this simulation, the fragmental pore phase area was not significantly greater than the cross sectional area of a cylindrical pore which expresses an inter-particle pore on a membrane. This was due to limitations in the size of the simulation cell. Therefore, voids less than 4 Å could not be an effective pore for permeation. Even for an amorphous silica structure, it should be noted that all gas species permeated dominantly through an identical cylindrical pore in our simulation.

3.2 Gas permeation simulation

3.2.1. Snapshots of permeation through a membrane of 8 Å pore

An actual observation of the appearance of molecular transport within a subnano-scale pore would be very useful in terms of clarifying the image of the phenomenon and to develop a qualitative understanding. Figures 7(a) – (e) show snap shots for helium and CO_2 permeation at different temperatures through an 8 Å pore. Each figure expresses a view of a vertical section of the simulation cell in the *y*-*z* plane at $x = 0$. Gas molecules permeate through the pore from the left side to the right. The upstream pressure was 2 MPa and the downstream region was evacuated.

Figure 7(a) and (b) show the permeation of helium molecules, with the LJ potential parameters listed in Table 1. The ε parameter is relatively small and helium has little interaction with the pore surface. On the other hand, Figs. (c) – (e) show data for CO_2 molecules. They have a larger interaction with the pore surface than helium. No striking difference in helium permeation at 260 K and 500 K can be seen. Helium molecules appear to permeate as normal gas molecules at both temperatures. On the contrary, CO_2 permeation is temperature dependent, and the concentration of permeating molecules increases with decreasing temperature. Especially, at 260 K, the concentration of molecules was clearly higher than that of the upstream gas phase outside the pore. These results suggest that interactions between permeating gas molecules and the pore surface play an important role in determining permeation properties through a micropore.

3.2.2. Determination of permeation rate

Important information on the microscopic states of the system can be obtained from these snapshots, and we can also better understand macroscopic properties through such permeation simulations. One of the most interesting quantities of the system is the permeance at a given temperature and pressure conditions at the steady state. We can confirm the steady state of the system by counting the number of gas molecules in the simulation cell along with elapsed time. Figure 8 shows an example of the changes in the number of adsorbed CO_2 molecules with time at four different membrane positions at 300 K. The volumes of (b), (c), (d) in Fig. 8 are almost identical and are 1/3 the pore volume. That is, the length of each part in the z-direction is 9.5 Å because the membrane thickness (pore length) is 28.5 Å. Therefore, the comparison in fig. 8 is similar to the comparison of local density. However, concerning (a), the membrane surface part, since its volume is different from (b)-(d), the comparison of adsorbed molecules in (a) with those in (b)-(d) is meaningless. It can be assumed that a steady state would be achieved when the number of adsorbed molecules reaches a constant

value. As shown in the figure, the number of adsorbed molecules gradually became stable from the upstream side towards the downstream side. This suggests that resistances to molecules transported through the pore exist, as well as from the membrane surface into the upstream pore. It appears that the system reached a steady state at around 600 ps, when the number of molecules in the downstream pore became stabilized.

We can also determine whether the system has reached a steady state or not by counting the number of gas molecules that permeat through a pore. Figure 9 shows the accumulated number of permeated molecules with lapsed time. This is an example of the case of CO_2 molecules. A linear relation between the number of permeated molecules and time can be seen at any temperature. These gradients were nearly constant and independent of time after 1000 ps, and we could therefore confirm that the system had reached a steady state. Since the slope of the curve indicates the permeation rate, it is obvious from this figure that the permeance increased with decreasing temperature.

3.2.3. Temperature dependency of permeance

Figure 10 shows Arrhenius plots of simulated permeance, which is the permeation rate divided by the apparent pressure drop across the membrane, at a steady state for an 8 Å pore. The values for permeation rate were obtained by counting the number of molecules for a certain period, about several *nano seconds*, during the steady state.

The *permeation flux* values at a lower upstream pressure, p_u = 0.2 MPa, were smaller than those at p_u = 2 MPa. However, the *permeance* was nearly independent of upstream pressure. We also calculated helium permeance using the normal DCV-GCMD technique and nearly identical values of permeance were obtained. In addition, we examined the velocity distributions of molecules, which had rebounded on the membrane surface or permeated through the membrane and should be deleted at a control plane. Figures 11(a) - (d) show the observed velocity distribution for each component at a control plane in the upstream region for 7343 helium molecules (a-c) and in the downstream region for 277 molecules (d) at T = 300 K and p_u =2 MPa with theoretical curves based on Eqs. (5) and (6). We found that the values for v_x and v_y for these molecules were in good agreement with the satisfied Maxwell-Boltzmann distribution described by Eq. (5) at the given temperature. The velocity of their z (permeating direction) component also were in good agreement with the distribution predicted by Eq. (6) for ideal gas molecules passing through a plane in the bulk gas phase. These results support the validity of the MD simulation method for maintaining a constant upstream pressure based on an ideal gas assumption in an imaginary gas phase, even at a pressure of 2 MPa. We did not consider the effect of streaming velocity in constructing the theoretical curves in Fig. 11(c) and (d). Since the simulation results showed good agreement with these curves, the effect of streaming velocity might be sufficiently small to be negligible in this system. However, we have not examined this aspect in detail yet.

As shown in Fig.10, the temperature dependency for helium permeance was not striking, while CO_2 permeance showed an obviously larger temperature dependency curve. In general, the permeation flux of gases, J, in the z direction can be given by the widely known Eq. (8) [3],

$$J = -Bc\frac{d\mu}{dz} = -D'\frac{d\ln p}{d\ln c}\frac{dc}{dp}\frac{dp}{dz}, \tag{8}$$

where, μ is the chemical potential, B the mobility, c the concentration, and D' the corrected diffusion coefficient given by Eq. (9),

$$D' = \rho_g \bar{v}\lambda = \rho_g\left(\frac{8RT}{\pi M}\right)^{0.5}\lambda, \tag{9}$$

where, ρ_g is governed by geometrical factors, $\bar{v}$ the mean molecular velocity and λ the mean free path. The permeance, P, can be given using the apparent pressure drop Δp and the diffusion length L by $P = JL/\Delta p$. In the case of the permeation of non-adsorbable molecules,

$$\frac{d\ln p}{d\ln c} = 1, \quad \frac{dc}{dp} = \frac{1}{RT}, \tag{10}$$

and we have the classic Knudsen permeance P_K described as Eq. (11) with parameter k_g, which is only dependent on pore geometry.

$$P_K = \frac{k_g}{(MRT)^{0.5}}, \tag{11}$$

If we dare to suppose a homogeneous potential field E_P as the first approximation for a leveled potential profile in both the radial and lateral directions within a micropore, the relation between the concentration in the pore, c, and the pressure outside, p, can be described as $cRT = p\exp(-E_P/RT)$ based on the Boltzmann distribution theorem,

$$\frac{d\ln p}{d\ln c} = 1, \quad \frac{dc}{dp} = \frac{1}{RT}\exp\left(\frac{-E_P}{RT}\right). \tag{12}$$

Accordingly, the permeance P_P in a potential field E_P would be given by the form of Eq. (13) [2],

$$P_P = \frac{k_g}{(MRT)^{0.5}}\exp\left(-\frac{E_P}{RT}\right). \tag{13}$$

The mechanism of permeation in a micropore is different from the simple Knudsen mechanism, probably because the interaction between a molecule and the pore wall surface influences the permeation properties of the gas. The permeation ratio, based on the Knudsen permeation model, is inversely proportional to the square root of the molar weight ratio, and leads to $P_{CO2} / P_{He} = 0.30$. However, the simulated permeation ratio was larger at all temperatures, as shown in Table 2. In addition, the deviation from the Knudsen value became larger with decreasing temperature. This result suggests that the temperature dependency for the permeance is different from that predicted by the simple Knudsen mechanism. The same tendency has been observed in the permeation of an inorganic gas for actual silica membranes [2]. The mechanism of transport of gases through porous membranes is usually classified into Knudsen diffusion and surface diffusion. The gas transport equation which considers the total flow rate of gases as the sum of the gas-phase flow and the surface flow is a useful model for explaining the temperature dependency of gas permeance in several sizes of micropores and at a wide temperature range [27]. On the contrary, the model presented herein assumes Knudsen like diffusivity and a Henry type adsorption relation to express gas phase diffusion in a subnano-scale pore, where the distinction between the gas phase and the surface adsorption phase is obscure or meaningless. By considering the pore size and the permeating gas molecular properties (size and affinity) dependence of E_P in this model, it would be expected that a universal and comprehensive understanding of the permeation mechanisms could be obtained in a micropore from Knudsen and surface diffusion to activated diffusion [2].

The broken curve in Fig.10 indicates the temperature dependency curve predicted by the Knudsen model, where the value of k_g is given as an arbitrary value. Therefore, it has no meaning for its absolute value. The relative permeance could be predicted from the molar weight, however, a detailed pore structure, except for the roughly estimated pore size, was not investigated and we did not evaluate the geometrical parameters for Knudsen diffusion in this study. The prediction of the absolute value of permeance by considering the simulated pore

structure represents future work. The solid curves were fitted using by Eq. (13), and the fitting parameters are summarized in Table 3. The temperature dependency of helium was almost the same as the Knudsen's slope, but, for CO_2, it was obviously different from the Knudsen value. On the contrary, these fitted curves are in good agreement with simulated results both for helium and CO_2. Considering the fitted value of E_P, which indicates the strength of gas-pore surface interactions, the interaction was very small for helium and this leads to a Knudsen like permeation, while CO_2 had a large interaction with the pore surface and this might cause an enhancement in permeance and a larger temperature dependency. This result is consistent with the values for the given ε_{gs} parameters for helium and CO_2.

3.2.4. Potential and density profile in 8 Å pore

In order to examine the validity of the value of E_P, we calculated the "real" potential profile within a pore for the case of CO_2 molecules. The solid curve in Fig. 12 shows the lateral potential distribution, $\Psi(z)$ (J/mol) at the center of an 8 Å pore. The lateral potential distribution means the external potential profile along the z-direction (permeation direction) at $x = y = 0$ (pore center). The curves in Fig. 12 were calculated by summing the Lennard-Jones interaction potential between a permeating CO_2 molecule and O atoms on the membrane at the given location, z. The potential decreased along the lateral direction from the pore entrance to the central part of the pore. The horizontal solid line in the figure shows the value of E_P evaluated by applying Eq. (13) to the simulated temperature dependency for CO_2 permeance. The value of E_P, about -4670 J/mol, is in good agreement with the "real" potential depth in the pore.

We also examined permeation characteristics from the viewpoint of gas density in the pore. Figures 13(a) and (b)-(d) show the relative density profiles for permeating gas molecules in a lateral direction for helium and CO_2, respectively. The observed density was normalized by the theoretical density in the gas phase, p_u/k_BT, calculated using the set-point pressure and temperature at an upstream control plane. The values for the predicted relative density, $\exp(-E_P/RT)$, in the upstream side of the pore, for each temperature, are also shown in the figures. The value of the density, at any temperature, was almost unity and zero, respectively at a distance from the membrane surface in the upstream and downstream regions. This indicates that both of the two control planes successfully functioned to maintain the desired pressure gradient. Concerning helium, the enhancement in density in the pore is not so striking. On the contrary, concerning CO_2, the temperature dependency for the density enhancement in the pore can easily be seen. As shown in the snap shots, the density increased with decreasing temperature. In addition, at any temperature, the gas concentration near the pore entrance was higher compared to that of the upstream gas phase outside the pore, and it decreased along the lateral direction, approaching zero. At temperatures of 400 K and 600 K, the predicted values were in good agreement with the simulated gas density at the upstream side in the pore. At 260 K, however, the simulated density was much greater than the predicted value. This may be explained by considering the difference in the adsorption mechanism as Henry adsorption at a high temperature region and Langmuir type adsorption at a lower region, as previously reported in [19]. This is also supported by the slight but reliable deviation of the data point at 260 K from the fitted curve in Fig. 10.

The contribution of transport resistance at the pore entrance and through the pore to the total resistance for gas permeation is very interesting. Arya et al. reported on the importance of pore exit effects on gas permeation [28]. In our simulations, we were not able to separate the transport resistances at the three parts of the simulation cell. As shown in gas density profile in Fig. 13, however, a significant discontinuity in the density profile between the

upstream side pore outside and pore inside was not seen for either helium or CO_2 permeation. The value of helium density inside the pore is almost equal to the gas phase density, and the CO_2 density increased continuously from the upstream side of the membrane surface to inside the pore. Around the pore exit, these densities gradually decreased to zero. The density along the flow direction decreased continuously mainly "in the pore" for both gas species. Therefore, for gas permeation in this type of micropore, the Knudsen transport resistance in a pore, due to the collisions of gas molecules to the pore surface, seems to be dominant.

3.2.5. Pore size dependency of permeation properties

The mean potential depth in a micropore depends, not only on the permeating gas species but on the pore size as well. Correlations between permeation properties and pore size was studied by examining the temperature dependency for helium and CO_2 permeance in two types of simulation cells with different pore sizes. One was the 8 Å pore described above and the other was a slightly smaller 6 Å pore. The observed helium and CO_2 permeance through the 6 Å [23] pore is also shown in Fig.10. In comparison with the result for the 8 Å pore shown in Fig. 10, not surprisingly, the absolute values for permeance were larger for the 8 Å than for the 6 Å pore. In the case of helium, both curves for the 8 Å pore and for the 6 Å pore were almost the same as the Knudsen's slopes. Concerning CO_2, however, an obviously larger temperature dependency of permeance was observed for the 6 Å pore compared with the 8 Å pore at temperatures above 400 K. This is quantitatively shown as the difference between the values of the fitted E_P parameters in Table 3. This pore size dependency for CO_2 permeance can be explained as follows. Figure 14 shows a schematic image of the potential well in the micropores. In a smaller pore, the overlapping of the potential field by the close pore wall causes a deeper potential well. This indicates that permeating gas molecules experience a larger interaction with the pore surface in a smaller pore than in a larger one [29]. This pore size dependency for the potential in a micropore can be explained by the theoretical equations reported earlier for a cylindrical pore made of carbon graphite plane [30] and a homogeneous solid [31]. However, the pore surface of the amorphous silica model has an intrinsically heterogeneous structure, and the validity of applying these theoretical potential equations to the subnano-scale pore on the amorphous silica model used in this study is not clear. Therefore, we did not conduct a comparison of the simulation results with the theoretical equations. Instead, we calculated the "real" lateral potential distribution at the pore center for CO_2 in the 6 Å pore, as shown in Fig. 12 by a broken curve. The "real" potential was actually deeper in the 6 Å pore compared to the potential in the 8 Å pore, which would be predicted by the above theoretical potential equations qualitatively. In addition, the value of the fitted E_P parameter for CO_2 permeation through the 6 Å pore was in good agreement with the depth of the potential well. Accordingly, this potential gap probably caused the difference in the temperature dependency of the permeance. It should also be noted that the CO_2 permeance through the 6 Å pore was not so large at temperatures below 350K. This can be readily explained by the curve effect of the adsorption isotherm. This permeation mechanism has been discussed elsewhere [19].

4. Conclusion

We prepared "virtual amorphous porous silica membranes" and gas permeation simulations were conducted to study the gas permeation behavior through a micropore using the DCP-NEMD simulation method.

The simulated silica membrane cell prepared in this study by the melt-quench method had two surfaces and a cylindrical subnano pore. In spite of the peculiarity of the simulation cell, it assumed an amorphous silica structure. Potential functions, potential parameters and the

procedures for preparing a porous silica membrane unit employed, would be useful in studies of microscopic phenomena on not only membranes but also amorphous porous materials in a broad sense.

The dual control plane non-equilibrium MD (DCP-NEMD) technique employed in this study was able to successfully maintain a pressure gradient in the simulation system, which was confirmed through studies of gas phase density and the velocity distributions of guest molecules. The strong points of this method are that the calculation process for the GCMC routine can be reasonably omitted. These features of the DCP-NEMD method contribute to a reduction in the computational cost required to obtain accurate transport properties of guest molecules through narrow pores. This simulation method, however, should not be employed to directly control the chemical potential of a high density phase, such as a liquid phase. Care should be exercised in the simulation conditions of the system as to whether this technique is applicable or not. As far as this study is concerned, it was reasonable to control a gas phase of 2 MPa at room temperature by the DCP-NEMD method.

In the permeation of gas molecules through a micropore, the simulated permeation properties were dependent on temperature, gas species and pore size. The permeance increased with decreasing temperature. The greater interaction of CO_2 with the pore surface yielded a larger temperature-dependency curve for permeance than helium. This fact could be understood by examining the gas density in a micropore potential field. The density of gas molecules was enhanced by attractive interactions with the pore surface, and the density increased with decreasing temperature as can generally be seen in the physical adsorption phenomenon within a pore. The molecular permeation seemed to be caused by a gas density gradient in a pore as the substantial driving force. Accordingly, with increasing interactions, the permeance became larger and the temperature-dependency of the permeance became more striking. The deviation in observed permeance from that predicted by the Knudsen model can be explained quantitatively by considering the depth of the attractive potential which a permeating molecule experiences in a micropore. Since the potential depth in a micropore also depends on pore size, the permeation properties could be influenced by the pore diameter. However, at low temperatures, a reduction in permeance was observed. The Henry type density enhancement model in the gas state failed to predict the density in a pore and the permeance at these low temperatures, especially for the 6 Å pore model. Since the excluded volume of permeating molecules would prevent the gas density from being as large as the value predicted from $\exp(-E_P/RT)$, this might lead to a misunderstanding of the effective driving force for permeation. The molecular dynamics simulation is an ideal experimental system and has the potential for use in such studies.

References

[1] R. S. A. Lange, K. Keizer, A. J. Burggraaf, Analysis and theory of gas transport in microporous sol-gel derived ceramic membranes, J. Membr. Sci. 104 (1995) 81-100.

[2] T. Yoshioka, E. Nakanishi, T. Tsuru, M. Asaeda, Experimental studies of gas permeation through microporous silica membranes, AIChE J. 47 (2001) 2052-2063.

[3] A. B. Shelekhin, A. G. Dixon, Y. H. Ma, Theory of gas diffusion and permeation in inorganic molecular-sieve membranes, AIChE J. 41 (1995) 58-67.

[4] D. L. Meixner, P. N. Dyner, Characterization of the transport properties of microporous inorganic membranes, J. Membr. Sci. 140 (1998) 81-95.

[5] A. J. Burggraaf, Single gas permeation of thin zeolite (MFI) membranes: theory and analysis of experimental observations, J. Membr. Sci. 155 (1999) 45-65.

[6] G. S. Heffelfinger, F. van Swol, Diffusion in Lennard-Jones fluids using dual control-volume grand-canonical molecular dynamics simulation, J. Chem. Phys. 100 (1994) 7548-7552.

[7] P. I. Pohl, G. S. Heffelfinger, D. M. Smith, Molecular dynamics computer simulation of gas permeation in thin silicalite membranes, Mol. Phys. 89 (1996) 1725-1731.

[8] A. P. Thompson, D. M. Ford, G. S. Heffelfinger, Direct molecular simulation of gradient-driven diffusion, J. Chem. Phys. 109 (1998) 6406-6414.

[9] S. Furukawa, T. Shigeta, T. Nitta, Non-equilibrium molecular dynamics for simulating permeation of gas mixtures through nanoporous carbon membranes, J. Chem. Eng. Jpn. 29 (1996) 725-728.

[10] J. M. D. MacElroy, Nonequilibrium molecular dynamics simulation of diffusion and flow in thin microporous membranes, J. Chem. Phys. 101 (1994) 5274-5280.

[11] R. F. Cracknell, D. Nicholson, N. Quirke, Direct molecular dynamics simulation of flow down a chemical potential gradient in a slit-shaped micropore, Phys. Rev. Lett. 74 (1995) 2463-2466.

[12] M. Miyahara, T. Yoshioka, M. Okazaki, Determination of adsorption equilibria in pores by molecular dynamics in a unit cell with imaginary gas phase, J. Chem. Phys. 106 (1997) 8124-8134.

[13] T. Yoshioka, M. Miyahara, M. Okazaki, Capillary condensation model within nano-scale pores studied with molecular dynamics simulation, J. Chem. Eng. Jpn. 30 (1997) 274-284.

[14] P. I. Pohl and G. S. Heffelfinger, Massively parallel molecular dynamics simulation of gas permeation across porous silica membranes, J. Membr. Sci. 155 (1999) 1-7.

[15] L. Xu, T. T. Tsotsis, M. Sahimi, Nonequilibrium molecular dynamics simulation of transport and separation of gases in carbon nanopores. I. Basic results, J. Chem. Phys. 111 (1999) 3252-3264.

[16] S. Furukawa, T. Nitta, Non-equilibrium molecular dynamics simulation studies on gas permeation across carbon membranes with different pore shape composed of micro-graphite crystallites, J. Membr. Sci. 178 (2000) 107-119.

[17] H. Takaba, E. Matsuda, B. N. Nair, S. Nakao, Molecular modeling of gas permeation through an amorphous microporous silica membrane, J. Chem. Eng. Jpn. 35 (2002) 1312-1321.

[18] S. Wang, Y. Yu, Grand canonical Monte Carlo and non-equilibrium molecular dynamics simulation study on the selective adsorption and fluxes of oxygen/nitrogen gas mixtures through carbon membranes, J. Membr. Sci. 271 (2006) 140-150.

[19] T. Yoshioka, T. Tsuru, M. Asaeda, Molecular dynamics studies on gas permeation properties through microporous silica membranes, Sep. and Purif. Technol. 25 (2001) 441-449.

[20] T. Yoshioka, T. Tsuru, M. Asaeda, Condensable vapor permeation through microporous silica membranes studied with molecular dynamics simulation, Sep. and Purif. Technol. 32 (2003) 231-237.

[21] T. Yoshioka, T. Tsuru, M. Asaeda, Molecular dynamics study of gas permeation through amorphous silica network and inter-particle pores on microporous silica membranes, Mol. Phys. 102 (2004) 191-202.

[22] B. P. Feuston, S. H. Garofalini, Empirical three-body potential for vitreous silica, J. Chem. Phys. 89 (1988) 5818-5824.

[23] A. Brodka, T. W. Zerda; Molecular dynamics of SF_6 in porous silica, J. Chem. Phys. 95 (1991) 3710-3718.

[24] M. P. Allen, D. J. Tildesley, Computer Simulation of Liquids, Clarendon, Oxford, 1987.

[25] G. Arya, H. Chang, E. J. Maginn, A critical comparison of equilibrium, non-equilibrium and boundary-driven molecular dynamics techniques for studying transport in microporous materials, J. Chem. Phys. 115 (2001) 8112-8124.

[26] D. M. Ford, E. D. Glandt, Molecular simulation study of the surface barrier effect. Dilute gas limit, J. Phys. Chem. 99 (1995) 11543-11549.

[27] J. Karger, D. M. Ruthven, Diffusion in zeolites and other microporous solids, John Wily & Sons, New York, 1992.

[28] G. Arya, E. J. Maginn, H. Chang, Effect of the surface energy barrier on sorbate diffusion in $AlPO_4$-5, J. Phys. Chem. B 105 (2001) 2725-2735.

[29] H. Takaba, K. Mizukami, M. Kubo, A. Stirling, A. Miyamoto, The effect of gas molecule affinities on CO_2 separation from the CO_2/N_2 gas mixture using inorganic membranes as investigated by molecular dynamics simulation, J. Membr. Sci. 121 (1996) 251-259.

[30] C. Gu, G. Gao, Y. Yu, Density functional study of the adsorption and separation of hydrogen in single-walled carbon nanotube, J. Hydrogen Energy 29 (2004) 465-473.

[31] B. K. Peterson, J. P. R. B. Walton, K. E. Gubbins, Fluid behavior in narrow pores, J. Chem. Soc. Faraday Trans. 2 82 (1986) 1789-1800.

Figure captions

Fig. 1. Schematic diagram of the procedure used to prepare a virtual amorphous silica membrane unit.

Fig. 2. Schematic diagram showing the DCP-NEMD simulation cell.

Fig. 3. Perspectives of a crystal and a melt-quenched membrane unit with a cylindrical pore viewed through a pore from the upstream side. Atoms and atomic bonds are drawn as small dots and sticks, respectively.

Fig. 4. Radial distribution functions for melt-quenched vitreous silica (solid curve) and for cristobalite crystal relaxed at 300 K (broken curve).

Fig. 5. O-Si-O and Si-O-Si bond angle distributions for melt-quenched vitreous silica (solid curve) and for a cristobalite crystal relaxed at 300 K (broken curve). The equilibrium bond angles of the cristobalite structure are 109 ° for O-Si-O and 180° for Si-O-Si, respectively.

Fig. 6. Pore size distributions of amorphous (solid curve) and crystal silica (dashed line) structures containing a cylindrical penetrating 8 Å pore.

Fig. 7. Snap shots of helium (a, b) and CO_2 (c, d, e) permeation at different temperatures through an 8 Å pore. Each figure expresses a vertical section view of the simulation cell. The upstream pressure was 2 MPa (left side) and the downstream was evacuated (right side).

Fig. 8. Changes in the number of adsorbed CO_2 molecules with time at four different positions in the z-direction for a membrane with an 8 Å pore at 300 K. (a) upstream membrane surface, (b) pore inside in the upstream side, (c) central portion of the pore, (d) pore inside in the downstream side. The upstream pressure is 2 MPa.

Fig. 9. Cumulative number of permeated molecules with lapse of time. This is an example of CO_2 permeation through the membrane with an 8 Å pore at different temperatures under an upstream pressure of 2 MPa.

Fig. 10. Arrhenius plots of observed helium and CO_2 permeance for an 8 Å pore (open keys, circle: p_u = 2 MPa, square: p_u = 0.2 MPa) and for 6 Å pore (filled keys) [21]. The broken curve indicates the theoretical temperature dependency for permeance predicted by the Knudsen model with an arbitrary geometrical parameter. The solid curves are fitted with Eq. (13).

Fig. 11. Velocity distribution of v_x, v_y and v_z at a control plane in the upstream (a-c) and downstream (d) regions for the case of helium permeation at T = 300 K and p_u = 2 MPa. Solid curves are theoretical distributions based on Eqs. (5) (a, b) and (6) (c, d).

Fig. 12. Lateral potential distributions at the center of 8 Å (solid curve) and 6 Å (broken curve) pore. The horizontal solid lines in the figure indicate the value of E_P evaluated by applying Eq. (13) to the simulated temperature dependency of CO_2 permeance as shown in Table 3

Fig. 13. Relative density profiles for permeating gas molecules in the lateral direction for helium (a) and CO_2 (b, c, d). The upstream pressure is 2 MPa. The observed density is normalized by the set-point density of the gas phase at a control plane in the upstream region. The horizontal broken lines in Figs. (b), (c), and (d) indicate the predicted relative density, $\rho_P/\rho_g \exp(-E_P/RT)$, in the upstream side of the pore. The insets show close-up views of the upstream gas phase and inside the pore.

Fig. 14. Schematic images of the potential well in micropores. Broken lines indicate approximated potential profiles in micropores. Mean potential well in micropores: E_P(8 Å) > E_P(6 Å).

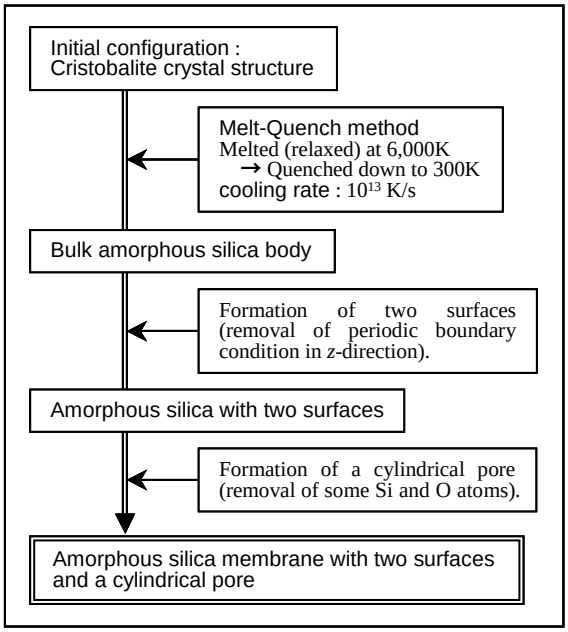

Fig. 1. Schematic diagram of the procedure used to prepare a virtual amorphous silica membrane unit.

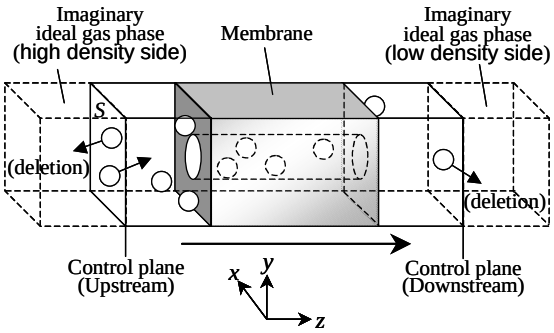

Fig. 2. Schematic diagram showing the DCP-NEMD simulation cell.

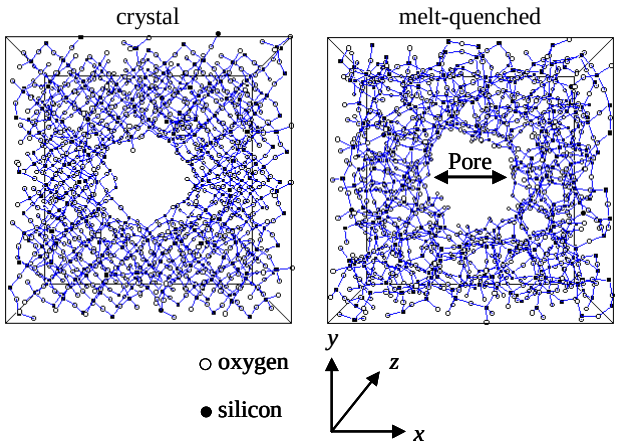

Fig. 3. Perspectives of a crystal and a melt-quenched membrane unit with a cylindrical pore viewed through a pore from the upstream side. Atoms and atomic bonds are drawn as small dots and sticks, respectively.

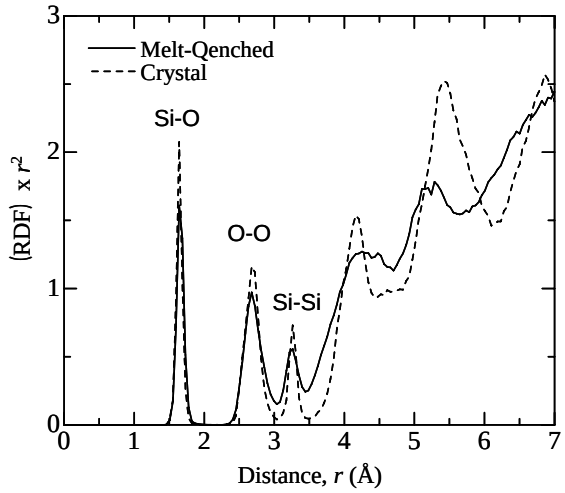

Fig. 4. Radial distribution functions for melt-quenched vitreous silica (solid curve) and for cristobalite crystal relaxed at 300 K (broken curve).

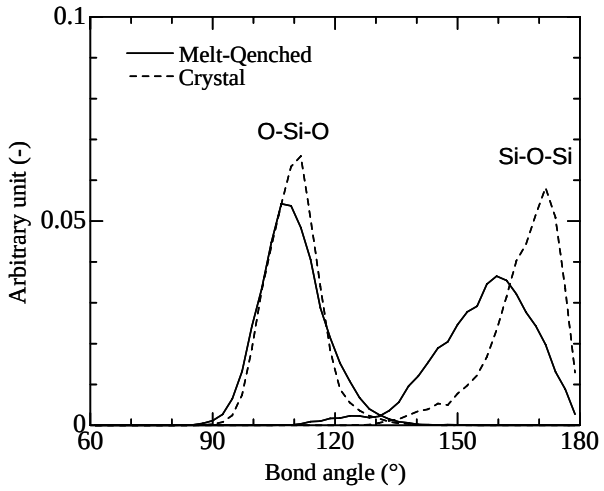

Fig. 5. O-Si-O and Si-O-Si bond angle distributions for melt-quenched vitreous silica (solid curve) and for a cristobalite crystal relaxed at 300 K (broken curve). The equilibrium bond angles of the cristobalite structure are 109 ° for O-Si-O and 180° for Si-O-Si, respectively.

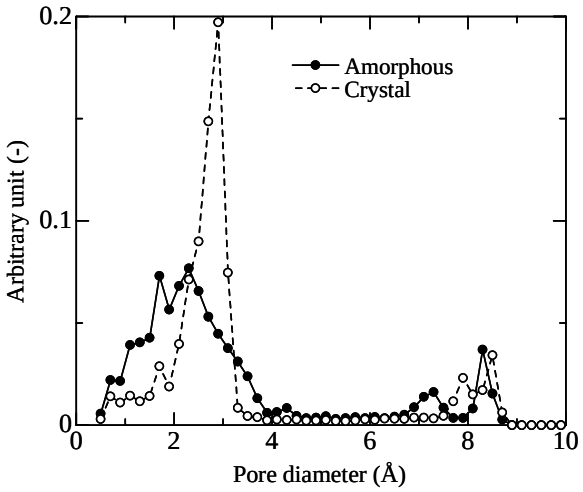

Fig. 6. Pore size distributions of amorphous (solid curve) and crystal silica (dashed line) structures containing a cylindrical penetrating 8 Å pore.

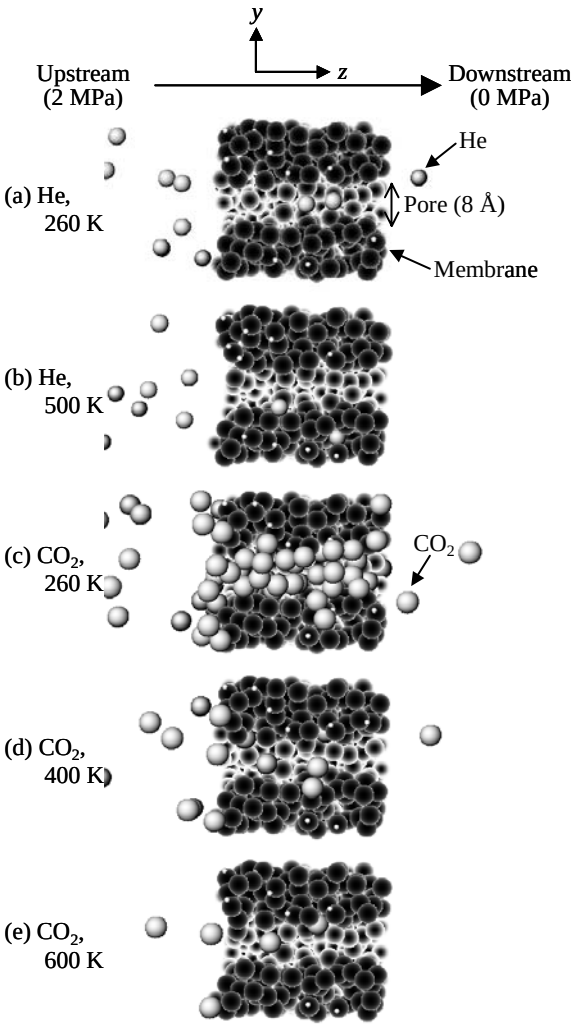

Fig. 7. Snap shots of helium (a, b) and CO_2 (c, d, e) permeation at different temperatures through an 8 Å pore. Each figure expresses a vertical section view of the simulation cell. The upstream pressure was 2 MPa (left side) and the downstream was evacuated (right side).

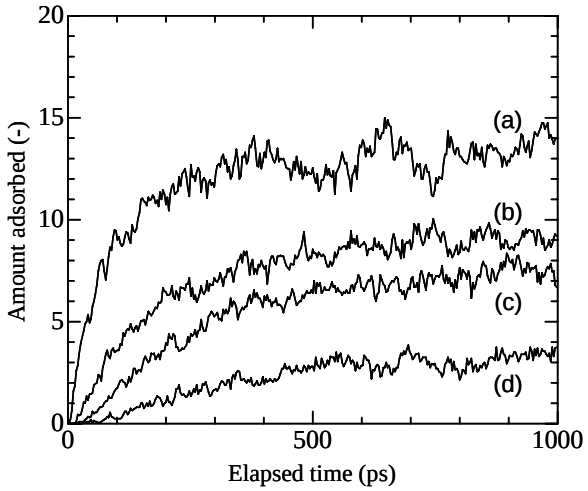

Fig. 8. Changes in the number of adsorbed CO_2 molecules with time at four different positions in the z-direction for a membrane with an 8 Å pore at 300 K. (a) upstream membrane surface, (b) pore inside in the upstream side, (c) central portion of the pore, (d) pore inside in the downstream side. The upstream pressure is 2 MPa.

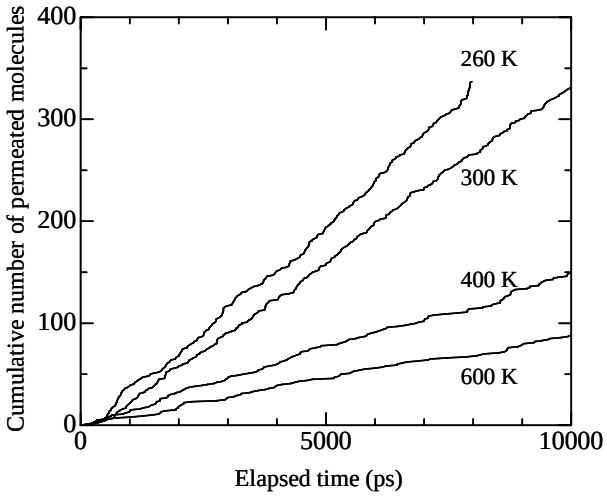

Fig. 9. Cumulative number of permeated molecules with lapse of time. This is an example of CO_2 permeation through the membrane with an 8 Å pore at different temperatures under an upstream pressure of 2 MPa.

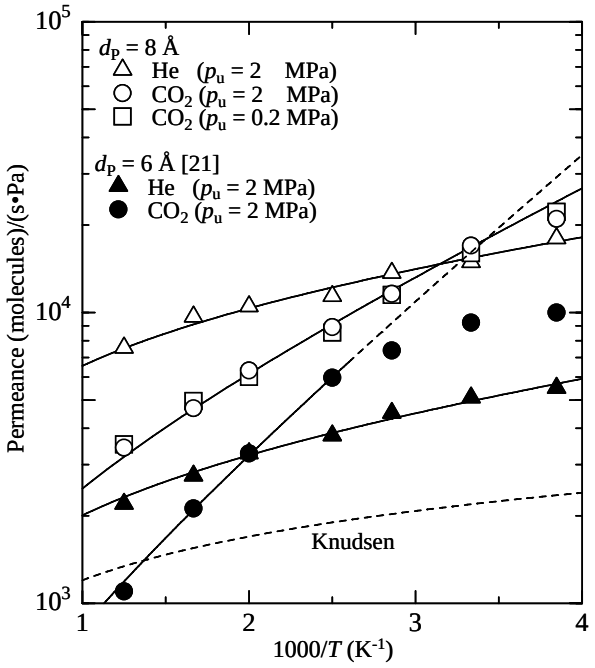

Fig. 10. Arrhenius plots of observed helium and CO_2 permeance for an 8 Å pore (open keys, circle: p_u = 2 MPa, square: p_u = 0.2 MPa) and for 6 Å pore (filled keys) [21]. The broken curve indicates the theoretical temperature dependency for permeance predicted by the Knudsen model with an arbitrary geometrical parameter. The solid curves are fitted with Eq. (13).

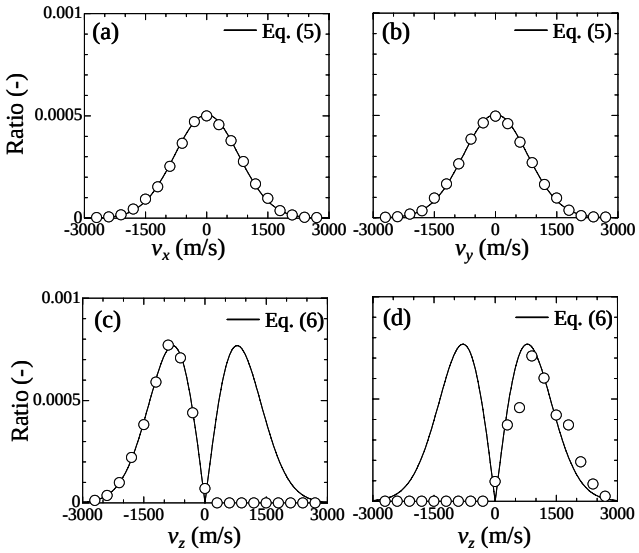

Fig. 11. Velocity distribution of v_x, v_y and v_z at a control plane in the upstream (a-c) and downstream (d) regions for the case of helium permeation at T = 300 K and p_u = 2 MPa. Solid curves are theoretical distributions based on Eqs. (5) (a, b) and (6) (c, d).

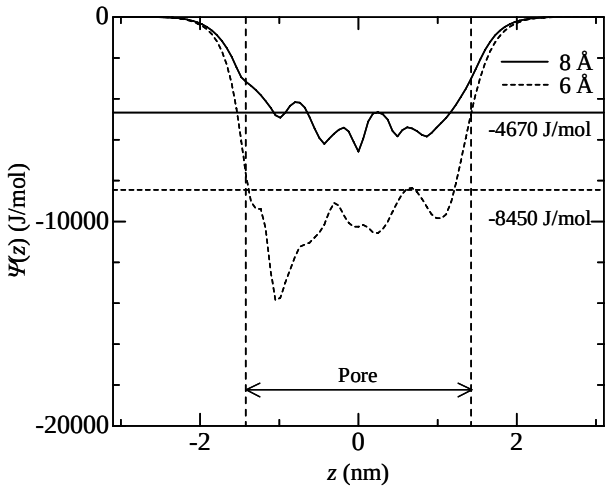

Fig. 12. Lateral potential distributions at the center of 8 Å (solid curve) and 6 Å (broken curve) pore. The horizontal solid lines in the figure indicate the value of E_P evaluated by applying Eq. (13) to the simulated temperature dependency of CO_2 permeance as shown in Table 3

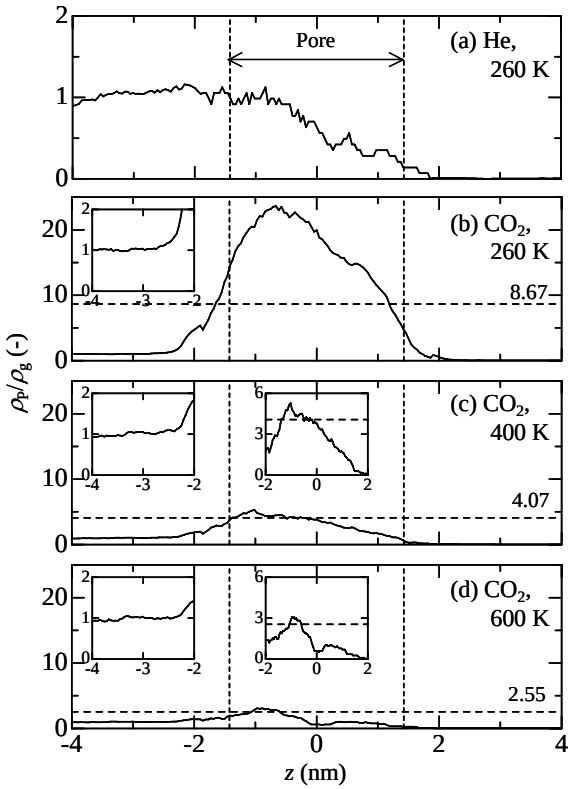

Fig. 13. Relative density profiles for permeating gas molecules in the lateral direction for helium (a) and CO2 (b, c, d). The upstream pressure is 2 MPa. The observed density is normalized by the set-point density of the gas phase at a control plane in the upstream region. The horizontal broken lines in Figs. (b), (c), and (d) indicate the predicted relative density, $\rho_P/\rho_g \exp(-E_P/RT)$, in the upstream side of the pore. The insets show close-up views of the upstream gas phase and inside the pore.

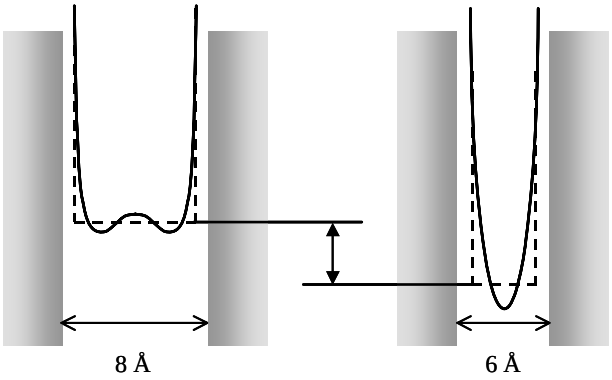

Fig. 14. Schematic images of the potential well in micropores. Broken lines indicate approximated potential profiles in micropores. Mean potential well in micropores: E_P(8 Å) > E_P(6 Å).

Table 1
Values of all potential parameters used in the present simulations.

Modified BMH		Si-Si	O-O		Si-O
	A_{ij} (10^{-16} J)	1.88 [a]	1.10 [a]		3.00 [a]
	β_{ij} (Å)	2.34 [a]	2.34 [a]		2.29 [a]
	ρ (Å)	0.29 [b]	0.29 [b]		0.29 [b]
SW		O-Si-O [a]			Si-O-Si [a]
	λ_i (10^{-18} J)	18.0			0.3
	γ_i (Å)	2.6			2.0
	r_i^c (Å)	3.0			2.6
	cos θ_{jik}	-1/3			-1
LJ		He [c]	CO_2 [c]	b-O [b]	nb-O [b]
	ε / k (K)	10.22	195.2	230	230
	σ (Å)	2.6	3.3	2.7	3.0

[a] Reference 18.
[b] Reference 19.
[c] Reference 3.

Table 2
Permeation ratios for helium and CO_2; P_{CO2} / P_{He}, where P_{He} and P_{CO2} indicate the permeance of He and CO_2 in (molecules)/(s·Pa), respectively.

T (K)	P_{CO2} / P_{He}		Knudsen $(M_{CO2}/M_{He})^{-0.5}$
	d_P = 8 Å	d_P = 6 Å	
800	0.45	0.50	
600	0.48	0.77	
500	0.60	1.00	
400	0.78	1.58	0.30
350	0.85	1.64	
300	1.14	1.81	
260	1.17	1.81	

Table 3
Values for k_g and E_P in Eq. (13) obtained from fitting to the observed temperature dependencies for the permeances shown in Fig. 10.

	E_P (J/mol)		k_g (-)	
	d_P = 8 Å	d_P = 6 Å	d_P = 8 Å	d_P = 6 Å
He	-900	-1060	3.39×10^{4}	1.02×10^{4}
CO_2	-4670	-8450	2.71×10^{4}	0.57×10^{4}